Advanced Powder Technology 31 (2020) 1333–1341

Contents lists available at ScienceDirect

Advanced Powder Technology

journal homepage: www.elsevier.com/locate/apt

Original Research Paper

Structural, electrical and electrochemical properties of ZnO nanoparticles synthesized using dry and wet chemical methods

M.G. El-Shaarawy [a], M. Khairy [b,c,*], M.A. Mousa [b]

[a] Physics Department, Faculty of Science, Benha University, Benha, Egypt
[b] Chemistry Department, Faculty of Science, Benha University, Benha, Egypt
[c] Chemistry Department, College of Science, Imam Mohammad Ibn Saud Islamic University, Riyadh, Saudi Arabia

ARTICLE INFO

Article history:
Received 24 October 2019
Received in revised form 26 December 2019
Accepted 8 January 2020
Available online 23 January 2020

Keywords:
ZnO
Nanoparticles
Electrical properties
Grain boundary
Supercapacitance

ABSTRACT

The effect of particle size and morphological structure on the electrical and electrochemical properties of ZnO (nanowires, nanorods, and nanospheres) prepared by two various routes: soft-wet and dry methods were investigated. The electrochemical performance is analyzed by cyclic voltammetric and galvanostatic charge–discharge measurements in 1 M KOH, whereas their electrical conductivity, and dielectric constant are measured by electrochemical impedance spectroscopy in a temperature range 293–383 K and frequencies from 10^2 to 10^7 Hz. All samples showed semiconducting behavior with conductivity values depending on the particle size and the morphological structure of the sample. The prepared samples showed supercapacitance behavior with capacitance values lie between 77 and 330 F g^{-1} and depend upon the morphological structure. The nanowire's structure showed the highest capacitance and good cycling stability. The high performance depends on the nanocrystalline size and the high surface area of the nanowire sample.

1. Introduction

Nano-sized particles own amazing physical and chemical properties and possess several potential applications in a widespread range of industrial divisions [1–5]. In nano-materials, the big surface to volume ratio as well as the presence of unlimited grain boundaries that occupy a great density of defects, have great effects on the physical properties such as electrical and electrochemical properties [5]. The nanomaterials offer several advantages in energy switching and loading applications, which comprise physical interaction and/or chemical reaction at the surface or boundary regions in the crystalline materials. Thus, the surface texture and surface energy and conductivity at the grain boundary play a very important role.

Nowadays more effective electrical storage is a demanding necessity to meet future social requisites. This need for more maintainable, efficient energy storage has motivated new scientific advanced capacitor designs in which nanotechnology are playing a serious role. Supercapacitors can match or substitute the batteries in electrical energy storage and gathering uses when great power delivery or uptake is required [6–11].

Supercapacitor behavior originates from the weighing scales between inner grain conductivity and grain boundary dielectric barrier. The properties of the supercapacitors mainly depend on the electrode materials by which they are made up of. In recent times, nanostructure-based electrode materials are focused enormously due to the properties of nano-materials such as enhanced diffusivity, greater electrical resistivity, a large fraction of atoms at the grain boundaries, and lower thermal conductivity. The increase in surface area of the nanomaterial causes an increase in the energy storage of the electrode. Generally, the transport of ions becomes simple once the distance between the electrode and electrolyte becomes smaller. Just a while ago, transition metal oxides, carbon materials and conducting polymers have been extensively accepted as electrode materials with outstanding capacitive properties [12–15].

Zinc oxide is an interesting metal oxide material owing to its distinctive physical and chemical properties, for example, the distinguished chemical and mechanical stability, a broad range of radiation absorption, high photocatalytic efficiency, non-toxic nature, etc. Zinc oxide is an n-type semiconductor with a significant energy gap of 3.37 eV [16]. The zinc oxide nanoparticles are used in different nanoscale devices e.g. ultraviolet lasers [17],

* Corresponding author at: Chemistry Department, Faculty of Science, Benha University, Benha, Egypt.
E-mail address: mohkhairy@fsc.bu.edu.eg (M. Khairy).

https://doi.org/10.1016/j.apt.2020.01.009

light-emitting diodes [18], flat panel display [19], photocatalysis and solar cells [20]. Zinc oxide is the topic of interest in these days due to its presence in much unique and important morphology like nanorods, nanoflowers, nanowires, nanodendrites and nanoparticles [21–25]. The ZnO nanoparticles can be prepared via different methods such as sol–gel [26], hydrothermal [27], precipitation [28], spray pyrolysis [29], and solid-state reaction [30].

We reported previously the preparation and characterization of ZnO with different morphological structures (nanorods, nanowires, and nanosphere) and studied the effect of both particle size and morphological structure on its optical and photocatalytic properties [31]. In continuation of our earlier research, this work was done to study and report the variation in electrical and specific capacitance with the change in particle size and morphological structure of ZnO by using impedance spectroscopy, cyclic voltammetry, and charge/discharge techniques.

2. Experimental

2.1. Materials and characterizations

The ZnO nanoparticles were prepared by wet and thermal dry methods reported in detail in our previous work [31]. In the wet method, we used a conventional precipitation method with and without CTAB surfactant. The prepared sample with surfactant denoted as Z_{CTAB} and that without surfactant denotes as Z_s. And in the dry method, ZnO nanoparticles were prepared by each of the oxidation of Zn metal and denoted as Z_o and by the thermal decomposition of zinc carbonate and denoted as Z_d. As explained in our previous work [31], during the formation process of ZnO, the CTAB surfactant act as a transporter of the particles and as a modifier that leads to the orientation growth of ZnO nanorods in (1 0 0) direction. Whereas, in the preparation of ZnO via oxidation of zinc powder by oxygen, ZnO is formed in the form of nanowire structure due to the difference in the growth rate of the prominent crystalline facets during the oxidation process. The surface energies of different hexagonal ZnO facets increases as (0 0 0 1) > (1 0 1 1) > (1 0 1 0) planes. Therefore, the growth rate of the (0 0 0 1) plane was the most rapid leading to the sharp formation of the nanowires [31].

The nanocrystalline powders were pressed into cylindrical pellets of 7 mm diameter and 2 mm thickness with a pressure of 0 0.3 Gpa for 3 min using a hydraulic press. Final densities of the pellets were measured by the Archimedes method. The particle size, morphological structure, density and surface area of the prepared samples are summarized in Table 1.

The density of pellets depends on the pressure used and thus their transport properties will be different from bulk properties. However, we used in our measurements the same pressure for making the pellets used in electrical measurements and the densities of the samples are not changed largely and in turn, the effect of pellet density on the electrical properties of the samples is not considered.

2.2. Electrical measurements

Two faces of the prepared pellets were coated with silver paste and sandwiched between two platinum electrodes. The temperature dependence of dc conductivity measurement was performed by Keithly (2400). The temperature dependence of dielectric constant (ε'), dielectric loss (ε''), and ac- conductivity (σ_{ac}) studies were done at a frequency range of 10^2–10^7 Hz using Fluke PM 6306 programmable automatic (RCL) bridge.

2.3. Electrochemical measurements

The working electrodes for the supercapacitor were prepared by making a paste of the ZnO nanoparticles with a binder polytetrafluoroethylene (1%, w/w) with the mass ratio 95:5 to form a thick paste. The paste was then regularly coated onto a sheet of precleaned indium tin oxide (ITO) glass (sheet resistance 18–20 Ω cm $^{-2}$) and dried at 100 °C. The electrochemical tests were performed in a three-electrode cell with a 1 M KOH aqueous electrolyte. A Pt mesh was used as a counter electrode and saturated calomel working as the reference electrode. The electrochemical analyses were carried out using a Gamry G750 potentiostat/galvanostat instrument with the EIS300 software.

3. Results and discussion

3.1. Electrical studies

A single crystal of ZnO is an n-type semiconductor that shows electrical conduction due to the presence of several defects mainly zinc interstitials and oxygen vacancies [32]. In the present work, the electrical properties of our samples were studied using dc- current and ac-impedance spectroscopy at a temperature range between 300 and 400 K. The dc – conductivity refers to the unidirectional flow of electric charge which traverses the entire conducting ZnO pellet when the pellet is mounted between two inert electrodes. Unlike the DC method which provides a global response of the sample, the AC method distinguishes between different mechanisms involved in the overall conductivity response of a material like grain conduction, grain boundary conduction, and electrode response.

The temperature dependence of dc- conductivity (σ_{dc}) for all samples are represented in Fig. 1a–g. The electrical conduction is found to follow the Arrhenius equation:

$$\sigma_{dc} = \sigma_{o,dc}\exp(-E_{dc}/k_bT) \quad (1)$$

where $\sigma_{o,\ dc}$ is the pre-exponential factor, $E_{a,\ dc}$ is the activation energy under dc-field and k_b is the Boltzmann's constant. The dc- conductivity data calculated from the slope of the linear fit of Arrhenius plots are listed in Table 2. The table shows that σ_{dc} is size-dependent and increases at room temperature as the particle size increases $Z_s > Z_d > Z_{CTAB} > Z_o$. However, this trend is changed by increasing the temperature due to the change occurring in each

Table 1
Particle Size, Morphological structure and surface textural data for ZnO samples.

Sample	TEM particle size (nm)	XRD particle size (nm)	Specific surface area S_{BET} (m^2/g)	Pore volume V_p (ml/g)	Pore size r (Å)	Density (g/cm^3)
Z_o	Nano wires (11; diam.), (300; length)	11	34.9	0.331	26.8	5.601
Z_d	24	21	22.5	0.321	23.1	5.602
Z_s	37	41	15.3	0.309	21.9	5.600
Z_{CTAB}	Nano rods (17; diam.), (80; length)	15	28.3	0.294	21.1	5.599

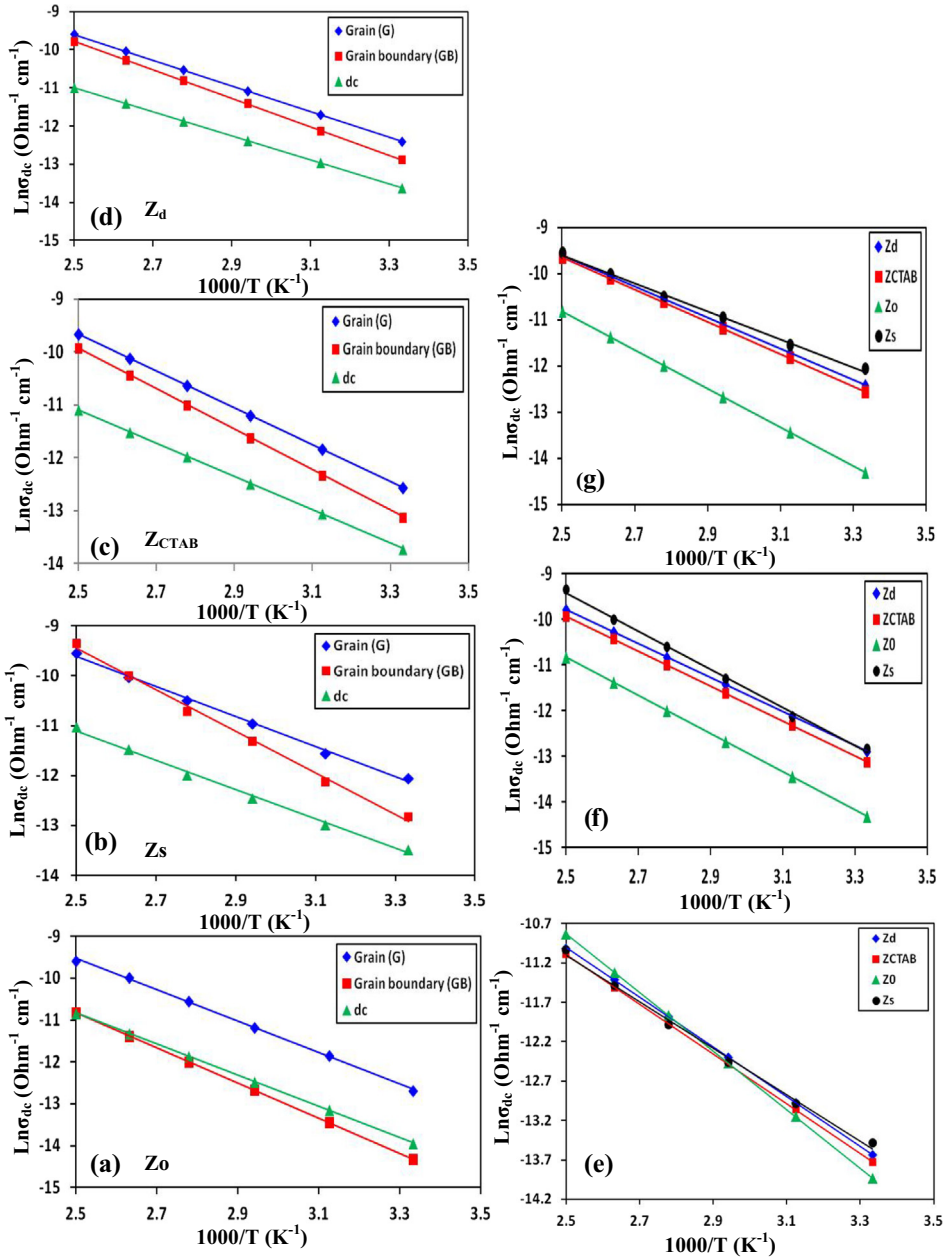

Fig. 1. The temperature dependence of dc-, grain (G)- and grain boundary (GB)-electrical conductivity of all samples.

Table 2
Electrical data of the studied ZnO samples.

Parameter	Z_o	Z_{CTAB}	Z_d	Z_s
XRD- Particle size (nm)	11	15	21	41
σ_g ($ohm^{-1}cm^{-1}$) × 10^6 at 300 K	3.1	3.5	4.1	5.8
$E_{a,g}$ (eV)	0.33	0.30	0.29	0.26
σ_{gb} ($ohm^{-1}cm^{-1}$) × 10^6 at 300 K	0.61	2.0	2.5	2.7
$E_{a,gb}$ (eV)	0.36	0.33	0.32	0.29
σ_{dc} ($ohm^{-1}cm^{-1}$) × 10^6 at 300 K	0.89	1.1	1.2	1.4
$E_{a,dc}$ (eV)	0.32	0.27	0.27	0.26
τ_{gb} × 10^4 (s) at 300 K	16.25	10.2	10.0	5.15
$E_{a,\tau,gb}$ (eV)	0.37	0.35	0.34	0.31
τ_g × 10^4 (s) at 300 K	3.2	5.8	6.1	2.4
$E_{a,\tau,\ g}$ (eV)	0.31	0.28	0.27	0.24
ε′ (at 300 K, 10 kHz)	115	104	100	46
ε′ (at 400 K, 10 kHz)	660	422	361	200
ε″ (at 300 K, 10 kHz)	60	58	55	40
ε″ (at 400 K, 10 kHz)	338	211	150	110

of the grains and grain boundaries in the investigated samples, as shown in Fig. 1e.

TEM results (Table 1) showed that the diameter of Z_{CTAB} (rods) is larger than that of (Z_o) wires, whereas the length of (Z_o) wires is larger than that of Z_{CTAB} (rods). And the conductivity results, shown in Fig. 1e illustrated that the dc-conductivity of Z_{CTAB} (rods) is larger than that of (Z_o) wires, at room temperature and vice versa at higher temperatures. This can be explained based on the presence of three kinds of resistance in the sample with wire structure, (i) the resistance of the wires, (ii) the wire—wire junction resistance, and (iii) the tunnel resistance between wires. All these resistance types increases as diameter decrease and length increase, which are affected by temperatures and in turn cause the variation observed in conductivity of the two samples with the change in temperature [33].

In nano metal oxides, the popular of ions are existing in the grain boundaries. These grain boundaries have significant density defects that modifying the electrical properties. To determine, the dynamics of bound or mobile charges in the interfacial and bulk region of our samples the ac-impedance spectroscopy technique was used. The investigation was carried out at a frequency range of 10^2–10^7 Hz and over a temperature ranging between 300 and 400 K. All samples showed similar behavior at different frequencies and temperatures. The typical Nyquist diagram (Z'' vs. Z') obtained at room temperature is shown in Fig. 2. Each plot shows two depressed semi-circles with centers lying below Z' axis, the first one appears in a low-frequency domain characterizes the resistance of grain boundary (R_{gb}) and the second one appears in a high-frequency domain corresponding to the resistance of grain (R_g). The resistances determined from the circular arc intercepts on Z' axis are found to hinge on the particle size and morphological structure of ZnO nanoparticles.

The capacitances of both grains (C_g) and grain boundary (C_{gb}) are derived from the circular arcs according to:

$$C_g = 1/(R_g \omega_g) \quad (2)$$

$$C_{gb} = 1/(R_{gb} \omega_{gb}) \quad (3)$$

where ω_g and ω_{gb} are angular frequencies for grains and grain boundaries at the semicircle peaks, respectively. And from which the corresponding relaxation times are calculated by $\tau_g = 1/\omega_g$ and $\tau_{gb} = 1/\omega_{gb}$.

The conductivity of grain (σ_g) and grain boundary (σ_{gb}) at different temperatures were calculated using the relations (4) and (5):

$$\sigma_g = 1/R_g \times (t/A) \quad (4)$$

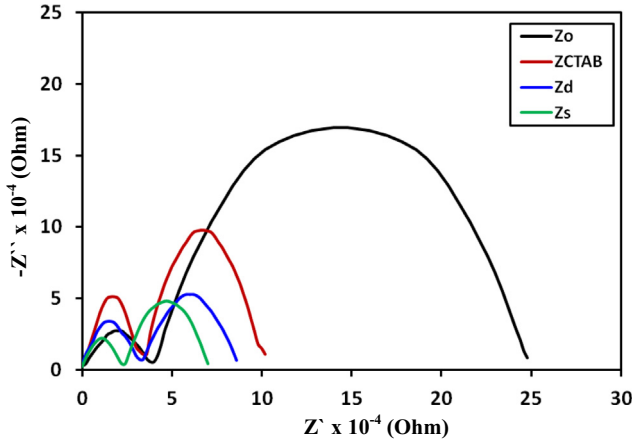

Fig. 2. Nyquist plots of Z''-Z' for ZnO samples.

where R_g , t, and A are the sample thickness and electrode area, respectively.

$$\sigma_{gb} = (\tau_g/\tau_{gb}) \times \sigma_g \quad (5)$$

τ_g and τ_{gb} are the time constants of the grain and grain boundary polarizations, respectively [34].

The temperature dependence of the grain and grain boundaries conductivity for all the studied samples showed Arrhenius behavior, as illustrated in Fig. 1a–g. The conductivity data for all samples are summarized in Table 2. It is evident from the figure that in spite of the dc-conductivity of all samples are not changed largely, but each of the grain and grain boundary conductivity of the Z_o sample (nanowire structure) showed higher conductivity values than those of other morphological structures. This can be explained on the basis that the native point defects are present in the bulk of ZnO nanowire and not just on their surface [35,36]. These defects inside nanowires and their metal junction can dominate the electrical contact properties, yet they can be moved by applied electric fields [37].

Relaxation times of the studied samples were found to decrease with increasing the temperature. The temperature dependence of relaxation time was found to follow the Arrhenius equation. The obtained data are summarized in Table 2.

The conductivity data obtained shows that σ_g is higher than that σ_{gb} and both are smaller than that recorded for ZnO single crystals (room temperature conductivity is ~10^{-3} $Ohm^{-1}cm^{-1}$) [38]. This can be explained based on the trapping of electrons by the localized states' interior or at the grain boundaries of nano-ZnO [39]. The grain boundaries possess a huge number of interface locations kept between the adjacent grains. These interface locations are created by dislocations offered by a crystallographic incompatibility between the neighboring grains, consequently achieving various interfacial defects [40]. Thus, bulk grains can be operated like a recompensed semiconductor with no– uniform spatial distribution [40]. This causes a collection of electrons at the grain boundary divisions leading to an enhancement in the grain boundary conductivity. In opposite to the ZnO single crystal, the majority of electronic trapping in ZnO nanoparticles is shallow [41,42]. The de-trapping process from such shallow is much simpler than that obtained from the deep levels in the ZnO single crystal leading to the smaller activation energy for the conduction process in nano-ZnO as shown in our results, Table 2.

The electrical conductivity (σ_{ac}) of the studied ZnO samples has been investigated at different temperatures over a frequency ranging between 10^2 – 10^6 Hz. The σ_{ac}-value was calculated from the relation [43].

$$\sigma_{ac} = (\cos\phi/Z') \times (l/A) \quad (6)$$

where ϕ is the phase angle. All samples show similar behavior for the frequency dependence of σ_{ac} (ω) at several temperatures, Fig. 3. One can note that the conductivity rises with the increase in frequency and temperature. Fig. 3a–d also shows that at low frequencies, conductivity displays the frequency-independent class of the sample. But, at the higher frequencies, σ_{ac} demonstrates frequency dispersion. Generally, the σ_{ac} (ω) of the studied samples at an individual temperature over a frequency range can be expressed as [44]:

$$\sigma_{ac}(\omega) = A\omega^n \quad (7)$$

where A is the temperature-dependent constant and n is the frequency exponent whose value and it's conducting with frequency and temperature decides the central conduction mechanism. The n values of the studied samples have been calculated using the slope of $\log\sigma_{ac}$ versus $\log\omega$ plots at various temperatures and found to be ranging between 0.15 and 0.5 and increase with reducing the

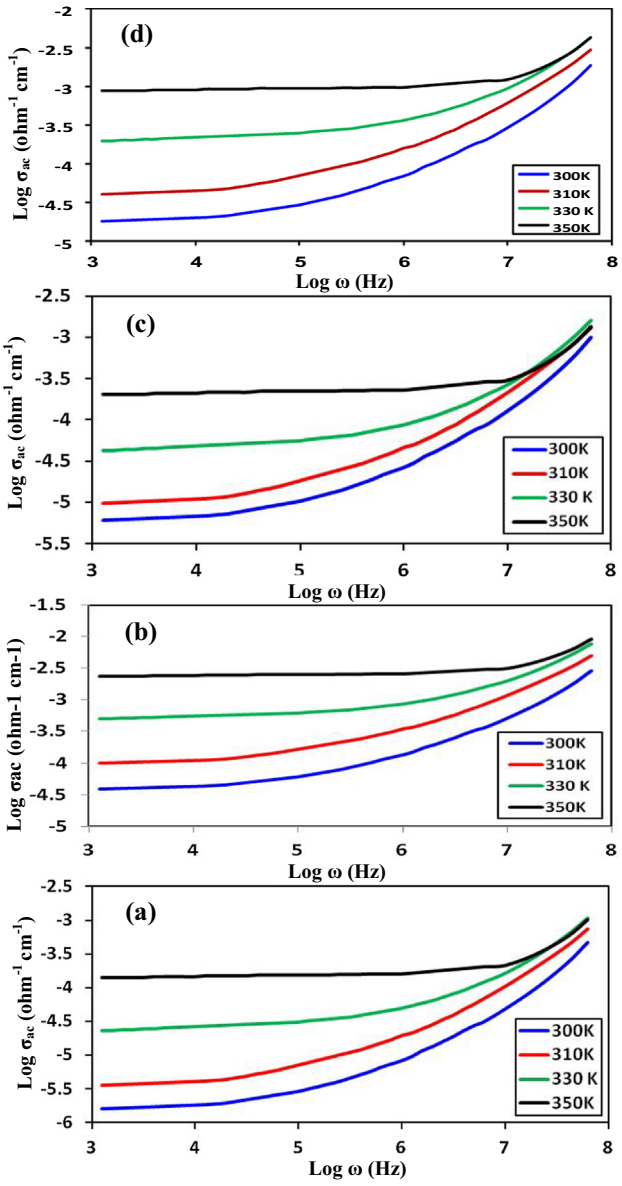

Fig. 3. AC- conductivity (σ_{ac}) versus applied frequency at various temperatures for (a) Z_o, (b) Z_s, (c) Z_{CTAB}, (d) Z_d.

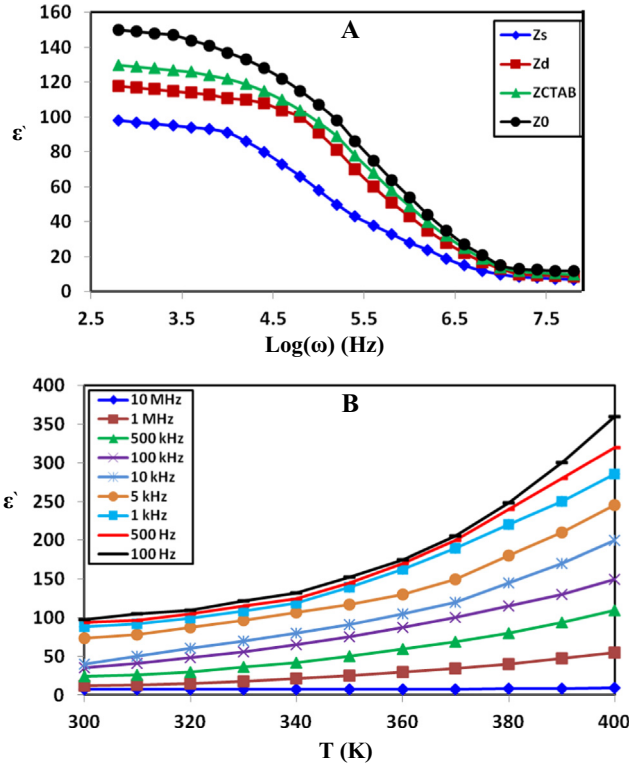

Fig. 4. (a) Relative permittivity ε′ vs. ac-frequency for the studied samples at room temperature. (b): Relative permittivity ε′ vs. temperature for the Z_s – sample at different frequencies.

temperature. This indicates that the correlated barrier hopping (CBH) model is the main conduction process in the investigated samples [45].

3.2. Dielectric properties

3.2.1. Dielectric constant

Grain boundaries operate as barriers for the cross transference of the charge carriers. Therefore, a comprehensive dielectric study, especially at grain boundary barriers, is essential for the investigated samples.

The relative permittivity of ZnO samples is calculated using equation (8):

$$\varepsilon = (C/\varepsilon_o) \times (l/A) \quad (8)$$

where ε_o is the permittivity of free space, $\varepsilon_o = 8.854 \times 10^{-12}$F/m.

The temperature and frequency dependence of the relative permittivity ε′ demonstrated analogous behavior for all the investigated samples; typical plots are shown in Fig. 4. A similar power-law dispersion is observed for the relative permittivity of each sample. The rapid increase in relative permittivity ε′ at lower frequencies, is at which all four types of polarization contribute, the rapid increase in dielectric constant is essentially attributed to space charge and dielectric polarizations, which are temperature dependent [46,47]. The plots of ε′ -log (ω) (Fig. 4a) show relatively high relative permittivity at low frequencies, which reduces with increasing the frequency. The ε′ - values can be produced from the contribution of deformation, dipolar and interfacial polarization [46]. Each of the interfacial and dipolar polarization is predominant in the low-frequency range [47]. In our nano ZnO, the volume fraction of the interfaces is about 10^{19} interfaces/cm^3, much bigger than those found in bulk ZnO [48,49]. Therefore, the space charge polarization produces in nano-ZnO and consequently, the dielectric constant will be higher than that of bulk ZnO. In our nano ZnO, a great number of positive oxygen vacancies [$V_{\ddot{o}}$] are produced in the huge number of interfaces present in the sample to be acting as shallow donors [40–42]. On applying the ac-electric field, the lot amount of the dipoles formed between O^- and $V_{\ddot{o}}$ are rotating. Where, at higher frequencies, the dipoles cannot be able to rotate suitably, hence their swinging will start to delay after the applied ac- field. Consequently, relative permittivity at high frequencies comes close to a limit value. On the other hand, at lower frequencies, the dipoles track the electric field producing a high ε′ value.

Fig. 4b demonstrates the dependence of ε′(ω) on the temperature at a frequency between10^2 to 10^7 Hz. It can be seen an enlarge in ε′(ω) with temperature. This trend is due to that the dipoles present in the nano-ZnO cannot orient themselves at low temperatures. Whereas with increasing the temperature, more and more dipoles will be oriented to develop the space charge polarization and in turn increases the dielectric constant [50]. More looking in Table 2, points to that the relative dielectric ε′- value changes

with both particle size and its morphological structure. The Z_o- sample with a wire structure exhibits the highest ε′- value.

3.2.2. Dielectric loss

The frequency and temperature dependence of the dielectric loss ε″ for the investigated samples show analogous behavior as that observed for the relative permittivity (ε_r), Fig. 5a. The obtained dielectric loss values are due to absorption a part of the electrical energy of the applied ac-field to overcome the internal friction forces between dipolar molecules through their reorientation along the direction of the electric field. At lower frequencies, the higher values of dielectric loss are attributed to the presence of space charge polarization as a result of charge lattice defects [51].

Fig. 5b shows a typical plot for the temperature and frequency dependence of ε″ of the Z_s sample. It shows a temperature-independent up to about 330 K, and after that, it increases with temperature. The obtained trend agrees with fairly accurate dispersion free high-frequency response, which recommends that the phenomenon is also connected to the space charge effect [52].

Both dielectric constant and dielectric loss changes largely with the change in each of the morphological structure and the porosity of the samples. Penn [53] reported that dielectric loss decreases with increasing the porosity as shown in our results.

3.3. Electrochemical study

The CV measurements were performed to deduce the specific capacitance of the investigated ZnO electrodes in 1 M KOH electrolyte using a three-electrode cell with Platinum foil used as the counter electrode and saturated calomel serving as the reference electrode. Fig. 6 presents the obtained cyclic voltammograms at a scan rate of 10 mV s^{-1}. The CV curves of all samples show a pair of redox peaks at ~ 0.29 V and 0.45 V (versus S.C.E), demonstrating

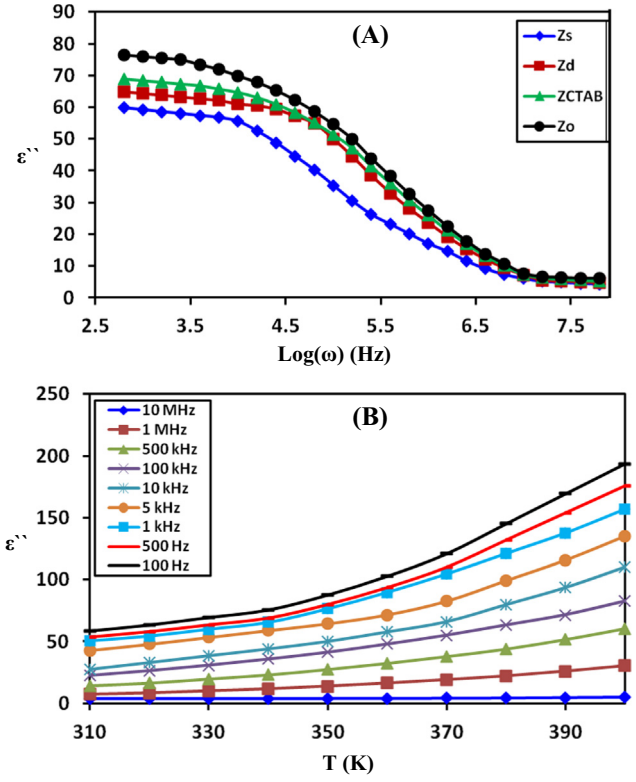

Fig. 5. (a) Dielectric loss ε″ vs. frequency for the investigated samples at room temperature. (b): Dielectric loss vs. temperature for the dielectric loss of Z_s –sample at different frequencies.

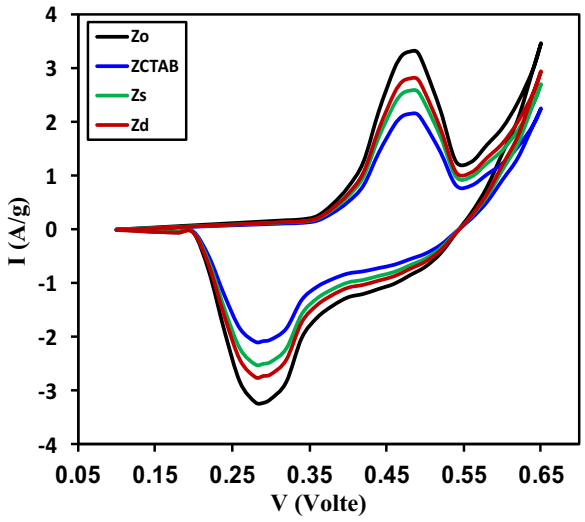

Fig. 6. Cyclic voltammetric curves for ZnO samples at a scan rate of 10 mV/s.

pseudocapacitive comportment. In the course of the Faradaic redox process, the intercalation and deintercalation of the K^+ ion taking place on the electrode surface are signified as [54,55]

$$ZnO + K^+ + e^- \leftrightarrow ZnOK \quad (9)$$

The redox peak current density and in turn the specific capacitance (C_{sp}) of the Zn electrode are found to increase in the order: $Z_o > Z_d > Z_s > Z_{CTAB}$. The specific capacitance of the electrodes is calculated from the CV curve by the next equation [56] and listed in Table 3:

$$Csp = \frac{\int i_v dV}{ms\Delta V} \quad (10)$$

where m is the mass of the active material on the electrode, *s* shows the potential scan rate, Δ V shows the sweep potential window and i_v is the voltammetric current on CV curves. Fig. 7 represents the CV curves of the Zn- (NW) electrode (highest capacitance, Z_o) at numerous scan rates ranging from 5 to 50 mV s^{-1}. As the scan rate increases, the total peak current also increases demonstrating the good rate properties and capacitance behavior.

The specific capacitance calculated from Eq. (10) is found to decrease with increasing the scan rate: 371, 347, 331, 312 and 211F/g for 5, 10, 15, 20 and 50 mv s^{-1}, respectively.

3.4. GCD study

The galvanostatic charge–discharge (GCD) measurements for the investigated ZnO electrodes were also studied to give more light on their electrochemical behaviors. Fig. 8 illustrates the GCD- curves of the different ZnO electrodes at a current density of 1 A g^{-1}. The discharge curves showed a non-linear trend owing to the pseudocapacitance character for the investigated samples.

The specific capacitance (C_{sp}) was calculated from the discharge curve using the following equation [57] and the results obtained are listed in Table 3:

$$C_{sp} = I_d t/\Delta V \quad (11)$$

where I_d is the discharge current density (A/g) and Δt is the discharge time(s). The specific capacitance obtained was found to increase in the order: Z_o (NW) > Z_d (nanosphere) > Z_s (nanosphere) > Z_{CTAB} (nanotube) as that observed from CV results. The GCD of ZnO (NW, Z_o) electrode with the highest capacitance was studied at different current densities of 1, 2, 4 and 8 A g^{-1}

Table 3
Supercapacitance data from CV curves GCD data for the ZnO samples.

Sample	C_{sp}(F/g) from CV curves at 10 mV s^{-1}	C_{sp}(F/g) from GCD data at 1 A g^{-1}	E (Wh/kg)	P (kw/Kg)
Z_o	347	330	15.13	0.31
Z_d	299	278	11.68	0.27
Z_s	267	254	11.64	0.30
Z_{CTAB}	81	77	3.53	0.25

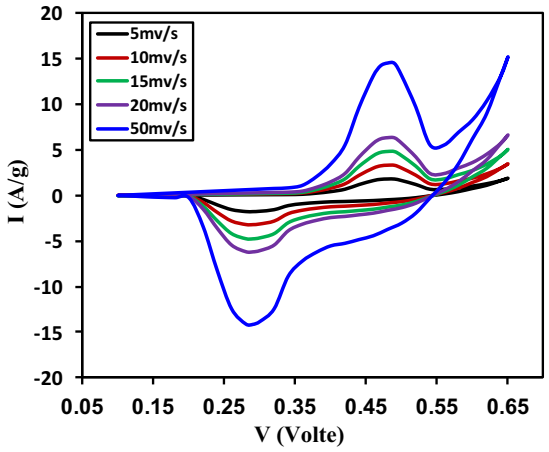

Fig. 7. Cyclic voltammetric curves for Z_o sample at different scan rates.

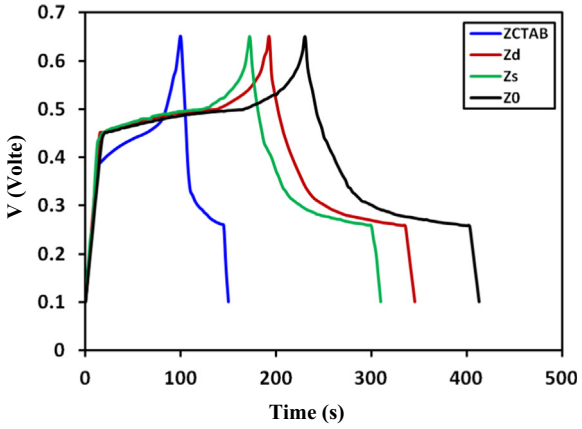

Fig. 8. GCD - curves at 1 A g^{-1} for ZnO samples.

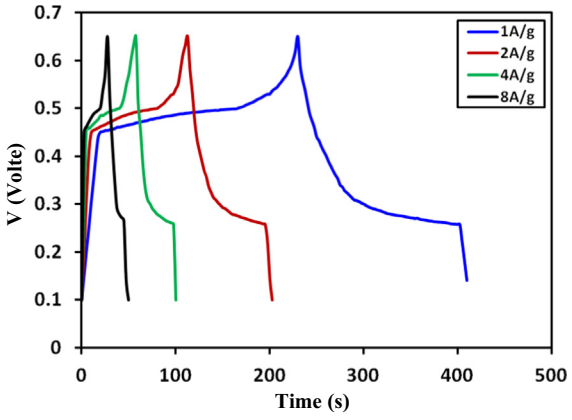

Fig. 9. GCD - curves for Z_o sample at various current densities.

(Fig. 9) and showed specific capacitance of 250, 237, 222, 214F g^{-1}, respectively. It has to be noted here that the changes in electrode sheet resistances at room temperature is not too high to induce the significant changes in the capacitance, and therefore, the latter can be attributed either to the morphology of the electrodes or to their surface areas. However, the obtained results showed that the variation in the specific capacitance with the change in the morphological structure differs from that observed for the variation in surface area, which increases in the order: $Z_o > Z_{CTAB} > Z_d > Z_s$ (Table 1). This means that the morphological structure plays an essential role in determining the capacitance value. It was found that the order of increasing capacitance matches the order of increasing both pore volume and pore size besides the different morphologies (sphere, wires, and nanotubes) of samples. So the high specific capacitance attributed to many factors (i) the mesoporous composition gives more tunnels which might quicken the diffusion of electrolyte ions inside the electrode; (ii) The spherical architecture of ZnO nanoparticles will be profitable for shortening transport way of ions and electrons. (iii) the morphological structure of animated material with the highest capacitance of wires structure with high surface area, pore volume and pore size enhance those contact zones between electrolyte and electrode, accordingly encouraging the transport of electrons to the current collector and electrolyte ions (OH–) flow inside the inner region of the electrode [58,59].

One of the most important parameters for supercapacitor operations is its long cycling stability. Thus, the electrochemical stability of the Z_o (NW) electrode (highest C_{sp}) was investigated at a current density of 1 A g^{-1}, which showed a retained about 92.2% of its first capacitance after 500 cycles, Fig. 10.

To further understand the electrochemical performances of the studied electrodes, the impedance measurements (EIS) were carried out in the same used electrolyte at a frequency ranging between 10^{-2} and 10^{6} Hz with an open circuit potential of 5 mV RMS. The obtained data are represented in Fig. 11. The crossing point on the Z-axis at the high-frequency section corresponds to the equivalent series resistance (ESR) [60] has values of 1.5, 1.8, 2 and 3.4 O for Z_o, Z_d, Z, and Z_{CTAB}, respectively. The low internal resistance of the NW sample (Z_o) is ascribed to the expanded sur-

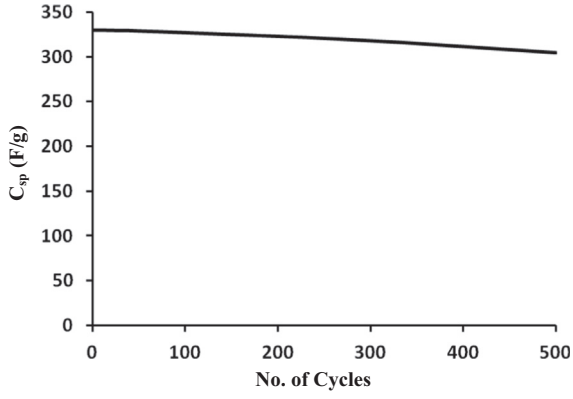

Fig. 10. Cycle stability of Z_o sample during 500 GCD cycling at a current density of 1 A g^{-1}.

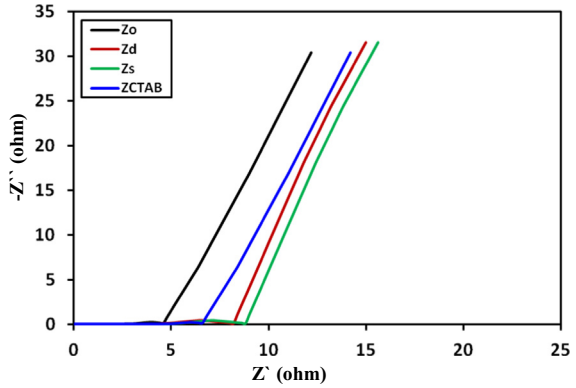

Fig. 11. Impedance spectra of different ZnO electrodes in 1 M KOH.

face area and increased the contact of the active material with the electrolyte. The diameter of the semicircle on the Z-axis corresponds to the charge transfer resistance on the electrode surface (R_{ct}) and found to be 1.6, 0.7,0.5 and 0.4 Ω for Z_o, Z_d, Z_s, and Z_{CTAB}, respectively.

The time constant (τ, s) of the capacitor has been calculated from the frequency (f°, Hz) at the maximum value of Z″ according to $\tau = 1/f°$ [61]. The obtained values are found to be 15.1, 25, 41, and 51 ms for Z_o, Z_d, Z_s, and Z_{CTAB}, respectively. The variation observed in the τ – value can be attributed to the difference in each of the particle size and morphological structure of the nano-ZnO. Low values of τ are desired for electrochemical capacitors for rapid charge–discharge processes [62].

Energy densities (E, Wh kg^{-1}) for the investigated capacitors were calculated using the following equation [15]:

$$E = 0.5C_{sp}(\Delta V)^2 \quad (12)$$

where C_{sp} is the capacitance value determined from the discharge of the GCD curve and V is the potential window. And the corresponding power density was calculated according to

$$P = E/\Delta t \quad (13)$$

The results obtained are listed in Table 3.

Maximum power density (P, Wkg^{-1}) was calculated by using the equation [63]:

$$Pmax = V^2/4ESR$$

The lower ESR will develop high power density through practical applications. Maximum power densities of supercapacitor are 41.66 kW/kg, 34.72 kW/kg, 31.25 kW/kg and 18.38 kW/kg for Z_o, Z_d, Z_s, and Z_{CTAB}, respectively.

4. Conclusion

The electrical conductivity, dielectric constant and capacitance behavior of ZnO with different morphological structure and particle size in the range of 11–41 nm have been studied. All different ZnO samples exhibit grain and grain boundary regions with different electrical properties depending on the particle size and morphological structure of the sample. The ac conductivity is explained according to the correlated barrier hopping (CBH) model. The dielectric results reveal that the dielectric response of ZnO nanoparticles is due to both the polarization of the ZnO-rotation direction and space charge polarization formed by plenty of oxygen vacancies and negative oxide anions present at the interfacial planes inside the nano-ZnO samples. The highest dielectric constant is found for the sample with a nanowire structure. The electrochemical study of the different ZnO samples showed specific capacitances ranging from 77 to 330F g^{-1} depending upon the morphological structure, and the best capacitance found for the nanowire structure with good cycling stability. EIS studies also confirmed that nanowire ZnO is respectable in supercapacitor application due to its minor charge transfer resistance (R_{ct}) compared with that of other morphologies In addition to its high surface area and large porous structure, which can offer comfortable charge moving across the material with stress-free lodging for ions from the electrolyte. The results obtained refer to that supercapacitors with greater charge storage can be devised across a nanostructure morphology selection strategy.

References

[1] P. Majzlíková, J.Sedláček, J. Prášek, J. Pekárek, V.Svatoš,1 Alexander G. Bannov, O. Jašek, P. Synek, M. Eliáš, L. Zajíčková, J. Hubálek, Sensing Properties of Multiwalled Carbon Nanotubes Grown in MW Plasma Torch: Electronic and Electrochemical Behavior, Gas Sensing, Field Emission, IR Absorption, Sensors 15 (2015) 2644–2661.
[2] F. Maglia, I.G. Tredici, U.A. Tamburini, Densification and properties of bulk nanocrystalline functional ceramics with grain size below 50 nm, J. Eur. Ceram. Soc. 33 (2013) 1045–1066.
[3] D.H. Kim, Effects of phase and morphology on the electrochromic performance of tungsten oxide nano-urchins, Sol. Energy Mater. Sol. Cells 107 (2012) 81–86.
[4] S.P. Jiang, Nanoscale and nano-structured electrodes of solid oxide fuel cells by infiltration: advances and challenges, Inter. J. Hydrogen Energy 37 (1) (2012) 449–470.
[5] J. Jeevanandam, A. Barhoum, Y.S. Chan, A. Dufresne, M.K. Danquah, Review on nanoparticles and nanostructured materials: history, sources, toxicity and regulations, Beilstein J. Nanotechnol. 9 (2018) 1050–1074.
[6] A. Eftekhari, On the mechanism of microporous carbon supercapacitors, Matr. Today Chem. 7 (2018) 1–4.
[7] C. Wang, E. Zhou, W. He, X. Deng, J. Huang, M. Ding, X. Wei, X. Liu, X. Xu, $NiCo_2O_4$-based supercapacitor nanomaterials, Nanomater. 7 (2017) 41.
[8] P.J. Hall, M. Mirzaeian, S.I. Fletcher, F.B. Sillars, A.J.R. Rennie, G.O. Shitta-Bey, G. Wilson, A. Cruden, R. Carter, Energy storage in electrochemical capacitors: designing functional materials to improve performance, Energy Environ. Sci. 3 (2010) 1238–1251.
[9] W. Li, L. Gan, K. Guo, L. Ke, Y. Wei, H. Li, G. Shen, T. Zhai, Self-supported Zn_3P_2 nanowires arrays grafted on carbon fabrics as an advanced integrated anode for flexible lithium ion battery, Nanoscale 8 (2016) 8666–8672.
[10] P. Sennu, V. Aravindan, Y.S. Lee, High energy asymmetric supercapacitor with 1D@2D structured $NiCo_2O_4$@ Co_3O_4 and jackfruit derived high surface area porous carbon, J. Power Sources 306 (2016) 248–257.
[11] D. Wang, K. Wang, L. Sun, H. Wu, J. Wang, Y. Zhao, L. Yan, Y. Luo, K. Jiang, Q. Li, S. Fan, J. Li, J. Wang, MnO_2 nanoparticles anchored on carbon nanotubes with hybrid supercapacitor-battery behavior for ultrafast lithium storage, Carbon 139 (2018) 145–155.
[12] A.M. Saleem, V. Desmaris, P. Enoksson, Performance enhancement of carbon nanomaterials for supercapacitors, J. Nanomater. (2016), https://doi.org/10.1155/2016/1537269,17 pages.
[13] H. Choi, H. Yoon, Nanostructured electrode materials for electrochemical capacitor applications, Nanomater. 5 (2015) 906–936.
[14] S. Faraji, F.N. Ani, The development supercapacitor from activated carbon by electroless plating-a review, Renew. Sustain. Energy Rev. 42 (2015) 823–834.
[15] M.A. Mousa, M. Khairy, M. Shehab, Nanostructured ferrite/graphene/polyaniline using for supercapacitor to enhance the capacitive behavior, J. Solid State Electrochem. 21 (2017) 995.
[16] P.B. Lihitkar, S. Violetb, M. Shirolkara, J. Singhc., O.N. Srivastavac, R.H. Naikb, S. K. Kulkarni, Confinement of zinc oxide nanoparticles in ordered mesoporous silica MCM-41, Mater. Chem. Phys. 133,(2012) 850–856.
[17] M. Ding, D. Zhao, B. Yao, E. Shulin, Z. Guo, L. Zhang, D. Shen, The ultraviolet laser from individual ZnO microwire with quadrate cross section, Opt. Express 20 (2012) 13657–21362.
[18] S.J. Pearton, F. Ren, Advances in ZnO-based materials for light emitting diodes, Curr. Opin. Chem. Eng. 3 (2014) 51–55.
[19] G.M. Nam, M.S. Kwon, Transparent conducting Ga-doped ZnO thin film for flat-panel displays with a sol-gel spin coating, J. Information Display 9 (2008) 8–11.
[20] W.Z. Wang, B.Q. Zeng, J. Yang, B. Poudel, J.Y. Huang, M.J. Naughton, Z.F. Ren, Aligned ultralong ZnO nanobelts and their enhanced field emission, Adv. Mater. 18 (2006) 3275–3278.
[21] N. Singh, P. Pandey, F.Z. Haque, Effect of heat and time-period on the growth of ZnO nanorods by sol-gel technique, Optik 123 (2012) 1340–1342.
[22] Y. Ling-min, F. Xin-hui, C. Lei, S. Jing-Yi, Y. Wen, Shape controlled cluster growth of ZnO nanoflowers using sol-gel method, Micro & Nano Letters, 7 (2012) 1046–1048.
[23] J. Cu, Zinc oxide nanowires, Mater. Charact. 64 (2012) 43–52.

[24] J.N. Hasnidawani, H.N. Azlina, H. Norita, N.N. Bonnia, S. Ratim, E.S. Ali, Synthesis of ZnO nanostructures using sol-gel method, Proc. Chem. 19 (2016) 211–216.
[25] Ch.-T. Wu, W.-P. Liao, J.-J. Wu, Three-dimensional ZnO nanodendrite/nanoparticle composite solar cells, J. Mater. Chem. 21 (2011) 2871–2876.
[26] Y.G. Wei, C. Xu, S. Xu, C. Li, W.Z. Wu, Z.L. Wang, Planar waveguide−nanowire integrated three-dimensional dye-sensitized solar cells, Nano Lett. 10 (2010) 2092–2096.
[27] C.M. Firdaus, M.S.B.S. Rizam, M. Rusop, S.R. Hidayah, Characterization of ZnO and ZnO: TiO_2 thin films prepared by sol-gel spray-spin coating technique, Proc. Eng. 41 (2012) 1367–1373.
[28] K. Byrappa, T. Adschiri, Hydrothermal technology for nanotechnology, Prog. Cryst. Growth Charact. Mater. 53 (2) (2007) 117–166, https://doi.org/10.1016/j.pcrysgrow.2007.04.001.
[29] O. Milosevic, B. Jordovic, D. Uskokovic, Preparation of fine spherical ZnO powders by an ultrasonic spray pyrolysis method, Mater. Lett. 19 (1994) 165–170.
[30] N.U. Sangari, S.Ch. Devi, Synthesis, and characterization of nano ZnO rods via microwave assisted chemical precipitation method, J. Solid State Chem. 197 (2013) 483–488.
[31] M.A. Mousa, W.A.A. Bayoumy, M. Khairy, Characterization and photo-chemical applications of nano-ZnO prepared by wet chemical and thermal decomposition methods, Mater. Res. Bullet. 48 (2013) 4576–4582.
[32] J.L. Zhao, X.M. Li, J.M. Bian, W.D. Yu, X.D. Gao, Structural, optical and electrical properties of ZnO films grown by pulsed laser deposition (PLD), J. Cryst. Growth 276 (2005) 507–512.
[33] I.V. Vodolazskay, A.V. Eserkepov, R.K. Akhunzhanov, Y.Yu. Tarasevich1, Effect of tunneling on the electrical conductivity of nanowire-based films: computer simulation within a core-shell model. arXiv:1911.02307v1 [cond-mat.mes-hall] 6 Nov 2019.
[34] X. Guo, W. Sigle, J. Maier, Blocking Grain boundaries in yttria-doped and undoped ceria ceramics of high purity, J. Am. Ceram. Soc. 86 (2003) 77–87.
[35] W.T. Ruane, K. Leedy, D.C. Look, G. Farlow, H. von Wenckstern, M. Grundmann, I.J. Brillson, Defect segregation and optical emission in ZnO nanowires and microwires, Nanoscale 8 (2016) 7631–7637.
[36] A. Jajour, J.W. Cox, W.T. Ruane, H. von Wenckstern, M. Grundmann, I.J. Brillson, Single metal ohmic and rectifying contacts to ZnO nanowires: A defect based approach., Ann. Phys. 530 (2018) 1700335.
[37] G.M. Foster, H. Gao, G. Mackessy, A.M. Hyland, M.W. Allen, B. Wang, D.C. Look, I.J. Brillson, Impact of defect distribution on IrO_x/ZnO interface doping and Schottky barriers, Appl. Phys. Lett. 111 (2017) 101604.
[38] A.R. Hutson, Piezoelectricity, and Conductivity in ZnO and CdS, Phys. Rev. Lett. 4 (1960) 505–507.
[39] J. Liu, X. Huang, J. Duan, H. Ai, P. Tu, A low-temperature synthesis of multiwhisker-based zinc oxide micron, Crystals Mater. Lett. 59 (2005) 3710–3714.
[40] Joshy Jose, M.Abdul Khadar, Impedance spectroscopic analysis of AC response of nanophase ZnO and ZnO-Al_2O_3 nanocomposites, Nanostruct. Mater. 11 (8) (1999) 1091–1099, https://doi.org/10.1016/S0965-9773(99)00399-2.
[41] P. Boguslawski, E.L. Briggs, J. Bernholc, Native defects in gallium nitride, Phys. Rev. B 51 (1995) 17255–17258.
[42] A.S. Lanje, S.J. Sharma, R.S. Ningthoujam, J.-S. Ahn, R.B. Pode, Low-temperature dielectric studies of zinc oxide (ZnO) nanoparticles prepared by precipitation method, Adv. Powd. Techn. 24 (2013) 331–335.
[43] Q. Huo, D.I. Margolese, U. Ciesla, D.G. Demuth, P. Feng, T.E. Gier, P. Sieger, A. Firouzi, B.F. Chmelka, F. Schuth, G.D. Stucky, Organization of organic molecules with inorganic molecular species into nanocomposite biphase arrays?, Chem. Mater. 6 (1994) 1176–1191.
[44] M. Pollak, T.H. Geballe, Low-frequency conductivity due to hopping processes in silicon, Phys. Rev. 122 (1961) 1742–1753.
[45] A.R. Long, Frequency-dependent loss in amorphous semiconductors Adv, Phys. 31 (1982) 553–637.
[46] A.K. Jonscher, Analysis of the alternating current properties of ionic conductors, J. Mater. Sci. 13 (1978) 553–562.
[47] G.K. Prajapati, P.N. Gupta, Conduction mechanism in un-irradiated and γ-irradiated PVA–H_3PO_4 polymer electrolytes, Nucl. Instrum. Methods Phys. Res. B 267 (2009) 3328–3832.
[48] S. Ramo, J. Winnery, T. Van Duzer, Fields and waves in communication electronics, 1st ed., John Wiley and Sons, New York, 1965.
[49] Y.P. Xu, W.Y. Wang, D.F. Zhang, X.L. Chen, Dielectric properties of GaN nanoparticles, J. Mater. Sci. 36 (2001) 4401–4403.
[50] G.J. Thomas, R.W. Seigel, J.A. Eastman, Grain boundaries in nanophase palladium: high resolution electron microscopy and image simulation, Scr. Metall. Mater. 24 (1990) 201–206.
[51] N. Izyumskaya, Y. Alivov, H. Morkoç, Oxides, oxides, and more oxides: high-κ oxides, ferroelectrics, ferromagnetics, and multiferroics, Crit. Rev. Solid State Mater. Sci. 34 (2009) 89–179.
[52] I. Levin, J.Y. Chan, J.E. Maslar, T.A. Vanderah, Phase transitions and microwave dielectric properties in the perovskite-like $Ca(Al_{0.5}Nb_{0.5})O_3$−$CaTiO_3$ system, J. Appl. Phys. 90 (2001) 904–914.
[53] S.J. Penn, N.M. Alford, A. Templeton, X. Wang, M. Xu, M. Reece, K. Schrapel, Effect of porosity and grain size on the microwave dielectric properties of sintered alumina, J. Am. Ceram. Soc. 80 (1997) 1885–1888.
[54] Y.L. Chen, Z.A. Hu, Y.Q. Chang, H.W. Wang, Z.Y. Zhang, Y.Y. Yang, H.Y. Wu, Zinc oxide/reduced graphene oxide composites and electrochemical capacitance enhanced by homogeneous incorporation of reduced graphene oxide sheets in zinc oxide matrix, J. Phys. Chem. C 2563–2571 (2011).
[55] X. Dong, Y. Cao, J. Wang, M.B. Chan-Park, L. Wang, W. Huang, P. Chen, Hybrid structure of zinc oxide nanorods and three-dimensional graphene foam for supercapacitor and electrochemical sensor applications, RSC Adv. 2 (2012) 4364–4369.
[56] Z. Fan, M. Xie, J. Xi Jin, T. Wei Yan, Characteristics and electrochemical performances of supercapacitors using double-walled carbon nanotube/δ-MnO_2 hybrid material electrodes, J. Electroanal. Chem. 659 (2011) 191–195.
[57] Z. Yang, C.Y. Chen, H.T. Chang, Supercapacitors incorporating hollow cobalt sulfide hexagonal nanosheets, J. Power Sources 196 (2011) 7874–7877.
[58] N. Zhao, H. Fan, M. Zhang, X. Ren, Ch. Wang, H. Peng, H. Li, X. Jiang, X. Cao, Facile preparation of Ni-doped $MnCO_3$ materials with controlled morphology for high-performance supercapacitor electrodes, Ceram. Intern. 45 (2019) 5266–5275.
[59] Q. Luo, P. Xu, Y. Qiu, Z. Cheng, X. Chang, H. Fan, Synthesis of ZnO tetrapods for high-performance supercapacitor applications, Mater. Lett. 198 (2017) 192–195.
[60] W. Cai, T. Lai, W. Dai, J. Ye, A facile approach to fabricate flexible all-solid-state supercapacitors based on $MnFe_2O_4$/graphene hybrids, J. Power Sources 255 (2014) 170–178.
[61] Y. Huang, Y. Liu, G. Zhao, J. Y. Chen, Sustainable activated carbon fiber from sawdust by reactivation for high-performance supercapacitors J. Mater. Sci. 52 (2017) 478–488.
[62] A. Burke, Ultracapacitors: why, how, and where is the technology, J. Power Sources 91 (2000) 37–50.
[63] R.R. Kotz, M. Carlen, Principles and applications of electrochemical capacitors, Electrochim. Acta 45 (2000) 2483–2498.